remote sensing

MDPI

Article

Radiometric Top-of-Atmosphere Reflectance Consistency Assessment for Landsat 8/OLI, Sentinel-2/MSI, PROBA-V, and DEIMOS-1 over Libya-4 and RadCalNet Calibration Sites

Sindy Sterckx * and Erwin Wolters

Flemish Institute for Technological Research (VITO)—Remote Sensing Unit, Boeretang 200, 2400 Mol, Belgium; erwin.wolters@vito.be

* Correspondence: sindy.sterckx@vito.be; Tel.: +32-14-33-68-19

Received: 19 August 2019; Accepted: 25 September 2019; Published: 27 September 2019

Abstract: There is a clear trend toward the use of higher spatial resolution satellite sensors. Due to the low revisit time of these sensors and frequent cloud coverage, many applications require data from different sensors to be combined in order to have more frequent observations. This raises concerns regarding data interoperability and consistency. The initial pre-requisite is that there are no radiometric differences in top-of-atmosphere (TOA) observations. This paper aims to quantitatively assess differences in the TOA signal provided by PROBA-V, Sentinel-2A and Sentinel-2B, Landsat-8, and Deimos-1 by using observations over both the Libya-4 desert calibration site and the RadCalNet sites. The results obtained over the Libya-4 site indicate that for all sensors investigated, the inter-sensor deviations are negligible, i.e., within ±2% for comparable spectral bands, with the exception of the Deimos-1 Green band. Clear BRDF (bi-directional reflectance distribution function) effects were observed over the RadCalNet sites, thereby preventing consistent conclusions on inter-sensor deviations from being made. In order to fully explore the potential of the RadCalNet sites, it is recommended that BRDF characterizations be additionally incorporated into the RadCalNet simulations and made publicly available through the distribution portal.

Keywords: radiometric calibration; RadCalNet; Libya-4; Landsat-8; Sentinel-2; PROBA-V; DEIMOS-1

1. Introduction

High spatial resolution satellite missions enable local operational earth observation (EO) services to be established. However, due to frequent cloud coverage, combined with the lower revisit time of higher spatial resolution sensors, operational services have to combine data from different sensors in order to collect observations of sufficient frequency. A seamless combination of EO data products obtained from different missions is not straightforward. The joint use of data from different sensors raises some clear concerns regarding data consistency. One of these is that there might be radiometric differences at TOA (top-of-atmosphere) level. Furthermore, even for a perfectly cross-calibrated constellation of instruments, intrinsic differences in the relative spectral response functions (RSRF) of spectrally comparable bands might cause discrepancies in the final products. Biases in the data products may also be introduced through the use of different processing chains and algorithms (e.g., for the atmospheric correction). One option is to normalize time series at product level, following an empirical approach. The drawback of such an approach is that the root cause of an observed bias is not identified. Furthermore, a non-linear empirical relationship could be identified with associated high uncertainty. Lastly, such an empirical relationship is only applicable to the sites and/or periods for which it has been derived.

In the harmonization of multi-mission high-resolution time series: Application to BELAIR (BELHARMONY) project [1], the aim is to obtain harmonized time series from Level 1 (L1) through value-added Level 3 (L3) bio-geophysical products for Landsat 8 (LS8) operational land imager (OLI), Sentinel-2 A/B (S2A/S2B) multi-spectral instrument (MSI), Project for On-Board Autonomy–Vegetation (PROBA-V), and Deimos-1 within the VNIR–SWIR spectral range. In BELHARMONY, a bottom-up approach (L1–L3) is used to assess and improve the consistency of multi-mission high-resolution time series. This bottom-up approach starts from the L1 TOA observations. This is important, as differences at L1 can be strongly amplified into L2 and L3 data products and should therefore already be corrected for at L1. Vicarious radiometric calibration methods are used to assess the consistency of the L1 TOA observations. Following the CEOS (Committee on Earth Observation Satellites) definition, "Vicarious calibration" refers to "techniques that make use of natural or artificial sites on the surface of the Earth for the post-launch calibration of sensors. These targets are imaged in near-coincident fashion by the sensor to be calibrated and by one or more well-calibrated sensors from satellite or aircraft platforms or on the ground".

The simultaneous nadir overpass (SNO) method [2] enables inter-sensor L1 cross-calibration. As highlighted in [3], an important limitation of the SNO approach is the need for simultaneous nadir observations of the sensors over the same target and strict constraints on the solar zenith and viewing zenith angles (SZA and VZA, respectively). Therefore, only a very low number of eligible image pairs are obtained, which becomes an even greater issue if more than two sensors are to be cross-calibrated, as in this case.

Another method of inter-sensor cross-calibration relies on the comparison of the sensor-measured TOA spectral reflectance ("MEAS") against modeled TOA ("REF") reflectance for a number of observations.

Ground-based reference surface reflectance spectra combined with atmospheric information, measured simultaneously with the satellite data acquisition, can be used as input to radiative transfer models (RTMs) in order to simulate/model the reference TOA reflectance values ("REF"), to which the sensor-measured values ("MEAS") are compared. Since the same reference approach is used for all instruments under investigation, the difference in the "MEAS/REF" ratio between the instruments is a direct measure of the inter-sensor calibration.

To increase the number of matchups between in-situ measurements and space sensor observations and to reduce the overall uncertainties, land equipped sites (LES) have been established. In-situ measurements are fully automated at these LES, thereby negating the presence of a field crew. To ease data access from LES, the RadCalNet, a radiometric calibration network of automated instruments, was established by a dedicated working group, with members from various international (space) organizations. RadCalNet comprises a set of four LES: National Aeronautics and Space Administration (NASA)'s site of Railroad Playa (USA, Lat: 38.497°, Long: −115.690°), Baotou (China, Lat: 40.85486°, Long: 109.6272°), the Centre d'Études National Spatiales (CNES) site of La Crau (France, Lat: 43.56, Long: 4.86°), and the European Space Agency (ESA)/CNES site in Gobabeb (Namibia, Lat: −23.59999°, Long: 15.119215°). The La Crau site, among others, has been used for vicarious calibration/validation of the modular optoelectronic multispectral scanner (MOMS)-2P-camera onboard the Russian MIR space station, the high-resolution visible (HRV) cameras on the Satellite Pour l'Observation de la Terre–Végétation (SPOT) satellites and Sentinel-2. In addition, the Railroad Valley site has been used for the calibration of various sensors, such as Landsat 8 OLI, Landsat 5 thematic mapper (TM), Landsat 7 enhanced thematic mapper plus (ETM+), the moderate-resolution imaging spectroradiometer (MODIS) onboard the Terra and Aqua satellites, the advanced spaceborne thermal emission and reflection radiometer (ASTER), the multiangle imaging spectroradiometer (MISR), and the constellation of RapidEye satellites [4].

In addition to the use of LES, 'pseudo invariant calibration sites' or PICS, usually corresponding to stable desert sites exhibiting high reflectance, can be used for inter-sensor cross-calibration [5,6]. A list of CEOS-endorsed PICS is included in [7]. Of these, the Libya-4 site has been shown to be one of the most stable sites and hence it is widely used.

The objective of this paper is to assess differences in the TOA signal provided by the various instruments (i.e., PROBA-V, S2A/S2B, L8, and Deimos-1) by using observations over both the Libya-4 desert site and the RadCalNet sites. The optical sensor calibration with simulated radiances (OSCAR) desert calibration approach [5] is used over Libya-4. As part of this approach, simulated TOA bidirectional reflectance factors (BRFs) define an absolute reference against which optical sensors can be cross-calibrated. In [5], the OSCAR Libya-4 site was used for the cross-calibration of low-resolution satellite missions, such as SPOT-VGT-2, MODIS-Aqua, the medium-resolution imaging spectrometer (MERIS), and polarization and anisotropy of reflectances for atmospheric sciences coupled with observations from a lidar (PARASOL). The same method is applied here. For the RadCalNet sites, the objective is to evaluate the extent to which the modeled nadir TOA hyperspectral reflectance data, which are publicly available through the RadCalNet portal, allow for inter-sensor cross-calibration.

We start with a brief overview of the sensors considered in the study (Section 2). Section 3 describes the OSCAR Libya-4 and RadCalNet methodology and data used. The results for both approaches are given in Section 3 and are discussed further in Section 4. Finally, conclusions are drawn in Section 5.

2. Satellite Missions

2.1. PROBA-V

The project for on-Board autonomy–VEGETATION (PROBA-V) is a small satellite, less than a cubic meter in size, designed to monitor global vegetation. It was launched on 6 May 2013 and was designed to bridge the gap in space-borne vegetation measurements between SPOT-VGT (March 1998–May 2014) and the two Sentinel-3 satellites, the first of which has been in orbit since 16 February 2016 and the second since 25 April 2018.

The VEGETATION instrument has a field of view of 102°, resulting in a swath width of 2295 km. This swath width ensures near-global daily coverage (90%), whereas full global coverage is achieved every two days. The optical design of PROBA-V consists of three cameras. The central camera (considered in this study) observes at 100 m nominal resolution and covers a swath of approximately 517 km, which ensures global coverage every five days. PROBA-V observes in four spectral bands: BLUE (centered at 0.463 µm), RED (0.655 µm), near infrared (NIR, 0.837 µm), and short-wave Infrared (SWIR, 1.603 µm, see Figure 1). Due to the lack of propellant onboard PROBA-V, the overpass time (10:45 at launch) decreases as a result of increasing atmospheric drag [8] and was 09:46 as of 24 September 2019. Due to the absence of on-board calibration devices, the radiometric calibration and stability monitoring of the PROBA-V instrument relies on vicarious and lunar calibration [9,10].

(a)

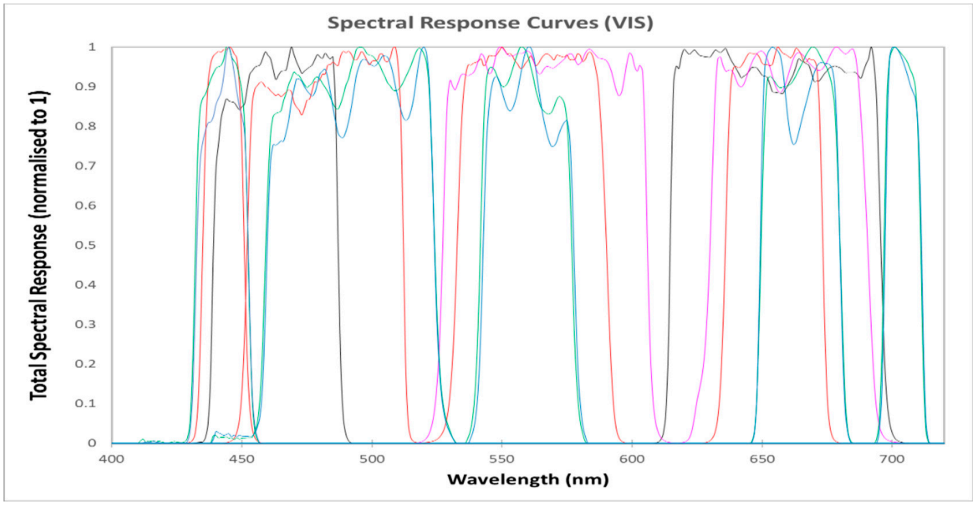

Figure 1. *Cont.*

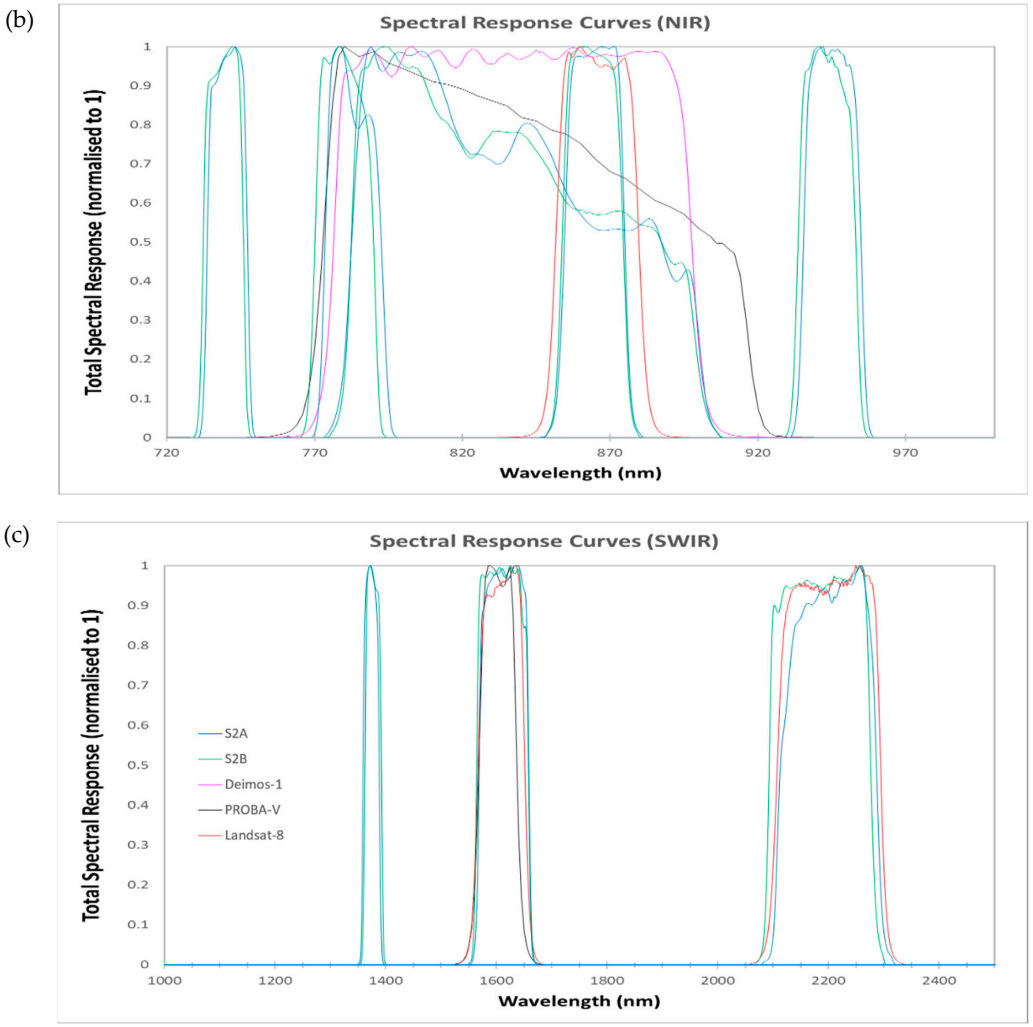

Figure 1. Spectral response curves for all sensors divided into three spectral ranges: (**a**) VIS (400–720 nm), (**b**) NIR (720–1000 nm), and (**c**) SWIR (1000–2500 nm).

2.2. DEIMOS-1

The DEIMOS-1 mission is fully owned and operated by Deimos Imaging (DMI, Spain). DEIMOS-1 was launched on 29 July 2009. The payload is the Surrey linear imager−6 channel−22 m resolution optical imager (SLIM-6-22). The SLIM-6-22 is a dual bank linear charged coupled device (CCD) push broom imager with 22 m ground sample distance (GSD) at a nominal altitude of 663 km, with a 625 km swath. The imager delivers observations in three spectral bands: RED (centered at 0.549 µm), GREEN (0.679 µm), and NIR (0.803 µm, see Figure 1). Deimos-1 lacks on-board calibration devices. In-flight radiometric calibration is performed through acquisitions over the Antarctic Dome-C site, the Pacific Ocean in eclipse, and PICS [11].

2.3. Sentinel-2

Sentinel-2 consists of a constellation of two satellites. Sentinel-2A (S2A) was launched on 23 June 2015 from Kourou, French Guiana. The S2A orbit had a mean local overpass time of 10:30. Sentinel-2B (S2B) was launched on 7 March 2017 from the same location as S2A. The twin satellites fly in the same orbit but are phased at 180° and provide a five-day repeat coverage.

Sentinel-2 carries the multi-spectral instrument (MSI) that samples in 13 spectral bands (Figure 1): Four bands at 10 m spatial resolution, six bands at 20 m, and three bands at 60 m. The orbital swath

width is 290 km. An on-board calibration device (OBCD) is used for the radiometric calibration of Sentinel-2 MSI.

2.4. Landsat-8

Landsat-8 (LS8) was launched on 11 February 2013. There are two imagers onboard: The operational land imager (OLI) and the thermal infrared sensor (TIRS). The OLI has nine spectral bands (Figure 1) covering the BLUE to SWIR wavelengths with a spatial resolution of 30 m for bands 1–7 and 9. The spatial resolution for band 8 (panchromatic) is 15 m. Landsat-8/OLI has a 16-day repeat cycle, with an equatorial crossing time of 10:00 ± 15 min. The OLI has three primary radiometric calibration devices built into its hardware: (1) A shutter, (2) lamps, and (3) solar diffusers. These are used in combination with lunar observations and terrestrial targets to provide the radiometric calibration of the OLI [12].

3. Methods and Data

3.1. OSCAR Libya-4

For the L1 TOA inter-comparison over the Libya-4 PICS desert site, we follow the OSCAR desert calibration approach described in [5], where it was successfully applied for the cross-calibration of low-resolution satellite missions. The OSCAR Libya-4 method relies on the comparison between cloud-free TOA reflectance as measured by the satellite sensor ("MEAS") and the modeled TOA reflectance values ("REF"). These modeled values serve as the 'absolute' calibration. The modeled TOA reflectance values are calculated with the Second Simulation of the Satellite Signal in the Solar Spectrum-Vector version (6SV) RTM using as input: Improved Rahman–Pinty–Verstraete (RPV) bi-directional reflectance distribution factor (BRDF) model [13] parameters derived from MODIS and MISR data by [5], following the approach originally described in [14]. Furthermore, European Centre for Medium-Range Weather Forecasts (ECMWF) numerical weather prediction (NWP) data (atmospheric pressure, total column ozone, and total column water vapor), a specific desert aerosol model derived for the Sahara region, a monthly variable aerosol optical thickness (AOT), based on an analysis of aerosol robotic network (AERONET [15]), and the terrain altitude are used as input. The modeled TOA reflectance values are simulated for the actual illumination and observation geometry and account for the instruments' actual spectral response. 6SV generates spectral TOA reflectance at 2.5 nm resolution. These are spectrally resampled to the S2A, S2B, LS8, Deimos-1, and PROBA-V spectral bands, considering the actual response curves of the sensors.

Among the six desert PICS sites endorsed by the CEOS/WGCV/IVOS subgroup (Committee on Earth Observation Satellites/Working Group on Calibration and Validation/Infrared and Visible Optical Sensors), the Libya-4 site has been shown one of the most stable sites [6]. However, the Libya-4 site is composed of long sand dune ridges that impact the surface BRDF as a function of the solar azimuth angle [16]. In order to account for these surface directional effects, BRDF models are traditionally used in the vicarious calibration methods [17]. In this study, the RPV BRDF model is used as described above.

The OSCAR Libya-4 calibration method has been applied to the S2A, S2B, LS8, Deimos-1, and PROBA-V TOA extractions over the Libya-4 ROI. Table 1 gives the number of cloud-free extractions used. All scenes were visually inspected from red–green–blue (RGB) quick looks to ensure that there were no undetected clouds or cloud-shadows at the site or in its vicinity (within ~5 km).

Table 1. Number of cloud-free Libya-4 extractions.

Platform	No. of Obs.
Sentinel-2A	68
Sentinel-2B	19
Landsat 8	62
PROBA-V	214
Deimos-1	91

3.2. RadCalNet

In order to evaluate biases of current and future satellite sensors in a harmonized manner, the RadCalNet has been established to facilitate traceability and sensor cross-comparison. RadCalNet comprises a set of four LES: Railroad Playa (USA, RVUS), Baotou (China), La Crau (France, LCFR), and Gobabeb (Namibia, GONA). The Baotou site was not included in this study, due to the small size of the representative area compared to the sensors' spatial resolution. GONA is situated in the gravel plains at the edge of the Namib Desert and was selected because of its high spatial homogeneity, low cloud coverage, relatively high surface reflectance stability, and stable atmospheric conditions [18]. LCFR is located in southeastern France, and its surface is uniformly covered by pebbles and dry grass-like vegetation. RVUS is located in Nevada (USA) in a dry lakebed or playa. Changes in the surface characteristics are generally due to rain and snow [18,19].

At the RadCalNet sites, surface and atmospheric data are automatically acquired. The RadCalNet data are publicly distributed through the RadCalNet portal [20]. Processed RadCalNet data distributed through the portal include modeled nadir TOA hyperspectral reflectance (at 10 nm spectral sampling resolution), including uncertainties at 30-min intervals from 09:00–15:00 local time (LT). The modeled nadir TOA hyperspectral reflectances are simulated using the moderate-resolution atmospheric transmission (MODTRAN-5) RTM and, after spectral resampling considering the sensors' RSRFs, these serve as a direct "REF" to compare the satellite-measured TOA signal with. It is important to highlight here that although BRDF measurements are performed at the sites, the RadCalNet portal only gives access to the nadir surface reflectance measurements and the corresponding nadir TOA reflectance simulations [21].

For each sensor, TOA reflectances were extracted or calculated for ~100 ×100 m regions centered at the RadCalNet sites' geolocation, which means 3 × 3 pixels for LS8, 5 × 5 pixels for S2A/S2B and Deimos-1, and a single pixel for PROBA-V. Subsequently, the sensor-measured TOA reflectances were compared to the corresponding simulated TOA reflectances, with a maximum time difference of ±30 min. To allow for direct inter-comparison to the measured TOA reflectances, the RadCalNet-simulated TOA reflectances provided at 10 nm spectral resolution were first interpolated to 1 nm resolution and then resampled to the S2A, S2B, LS8, Deimos-1, and PROBA-V spectral bands, taking into account actual their spectral response curves. To exclude any cloud contamination to the observed TOA reflectance RGB quick looks for all sensor observations were subjected to visual inspection upon acceptance.

Table 2 shows the number of cloud-free match-ups between the various TOA sensor observations and RadCalNet simulations over the three sites. It is clear that the sample sizes are relatively small and that, mainly over RVUS for S2B, Landsat-8, and Deimos-1, there are very few match-ups (< 10). For Deimos-1, only very limited cloud-free data acquisitions over LCFR and RVUS were available, while no data were available over GONA.

Table 2. Number of cloud-free matchups for the various sensors over the RadCalNet sites.

Sensor	LCFR	RVUS	GONA	Total
Sentinel-2A	32	14	27	73
Sentinel-2B	20	8	22	50
Landsat 8	24	6	14	44
PROBA-V	103	28	42	173
Deimos-1	4	7	0	11

The matchups between the sensor and simulated TOA reflectances were generally constrained by the availability of the RadCalNet simulations and the cloud occurrence over or in the respective sites' vicinity (< ~5 km). According to [4,22], typically only 25% of the LS8 acquisitions over the RVUS site are successful. Reasons for unsuccessful collections are clouds over the site or water/snow on the surface. For RVUS, the presence of efflorescent salts (i.e., the migration of a salt to the surface of a

porous material) after the site had dried out from a precipitation event also rendered images unsuitable for calibration purposes, due to the negative impact on the site's homogeneity.

4. Results

4.1. Libya-4

For each sensor and spectral band (excluding designated cirrus detection and strong water vapor absorption bands), the mean ratios (over all observations) of the satellite-measured TOA reflectances to the 6SV TOA reflectance simulations in comparison with S2A are plotted (see Figure 2 and Table 3).

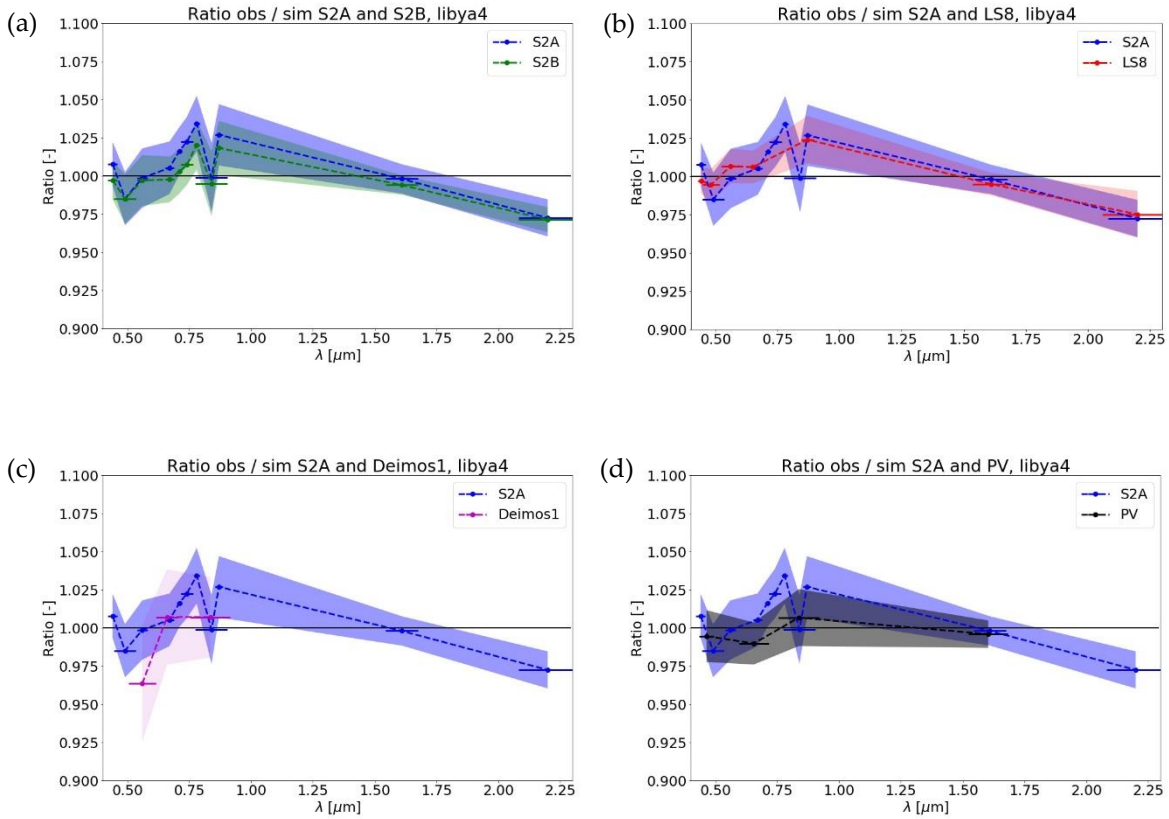

Figure 2. Mean ratio (over all observations) of the satellite-measured top-of-atmosphere (TOA) reflectances to the 6SV TOA reflectance simulations over Libya-4: (**a**) Sentinel-2A versus Sentinel-2B, (**b**) Sentinel-2A versus Landsat 8, (**c**) Sentinel 2A versus Deimos-1,and (**d**) Sentinel-2A versus PROBA-V. The shaded areas denote the ±1 standard deviation (σ) of the obtained ratios. The horizontal bars indicate the spectral band widths of the respective sensors.

The satellite-measured and simulated TOA reflectances agree to within ±4% for all sensors and spectral bands, and even to within ±2% for most bands. The largest deviation is observed for the Deimos-1 Green band, which is approximately 3.5% lower than the 6SV reference TOA reflectance.

In view of the BELHARMONY harmonization objective, we are mainly interested in relative differences between the sensors, rather than in the absolute reference. Therefore, it is more relevant to compare the results for spectrally similar bands. This also excludes issues attributable to possible intrinsic differences in the TOA reflectance simulations. We use S2A as the reference in the inter-comparison. Please note that using S2A as reference should not be interpreted here as implying that S2A has the highest absolute radiometric accuracy. The inter-comparison results are given in Table 4. Positive values for a certain band indicate that the sensor is brighter than S2A, while the opposite applies for negative values.

For comparable spectral bands, LS8, PROBA-V, S2B, and Deimos-1 agree with S2A to within ±2%, with the exception of the Deimos-1 Green band. Deviations observed between S2A and S2B are of the same magnitude as those observed between S2A and the other missions. For most bands, S2A is slightly brighter than S2B. This is in line with the findings of [23].

Table 3. Mean ratio (over all observations) of the satellite-measured TOA reflectances to the 6SV TOA reflectance reference simulations over Libya-4.

S2	S2	S2A	S2B	LS8	LS8	LS8	Deimos1	Deimos1	Deimos1	PV	PV	PV
band	cwv	ratio	ratio	band	cwv	ratio	band	cwv	ratio	band	cwv	ratio
1	443	1.008	0.997	CA	443	0.997						
2	490	0.985	0.985	Blue	492	0.994				Blue	460	0.995
3	560	0.999	0.997	Green	561	1.007	Green	549	**0.964**			
4	665	1.005	0.998	Red	654	1.006	Red	679	1.007	Red	658	0.990
5	705	1.016	1.003									
6	740	1.023	1.007									
7	783	1.034	1.020									
8	842	0.999	0.995				NIR	803	1.007	NIR	834	1.007
8A	865	1.027	1.018	NR	865	1.024						
9	945	NA	NA									
10	1375	NA	NA	Cirrus	1373	NA						
11	1610	0.998	0.994	SWIR1	1610	0.995				SWIR	1610	0.996
12	2190	0.973	0.971	SWIR2	2200	0.975						

Table 4. Cross-calibration results: Inter-comparison of the mean ratios for spectrally similar bands. The percentage difference of the mean ratios given in Table 3 for the different sensors to the ratios for Sentinel-2A for spectrally similar bands is provided. Positive values for a certain band indicate that the sensor is brighter than Sentinel-2A.

S2	S2	S2A	% dif S2B	LS8	LS8	% dif LS8	Deimos1	Deimos-1	% dif D-1	PV	PV	% dif PV
band	cwv	ratio	vs S2A	band	cwv	vs S2A	band	cwv	vs S2A	band	cwv	vs S2A
1	443	1.008	−1.05%	CA	443	−1.05%				Blue	460	−1.30%
2	490	0.985	−0.03%	Blue	492	0.94%					460	0.97%
3	560	0.999	−0.16%	Green	561	0.82%	Green	549	−3.5%			
4	665	1.005	−0.76%	Red	654	0.08%	Red	679	0.2%	Red	658	−1.55%
5	705	1.016	−1.32%									
6	740	1.023	−1.49%									
7	783	1.034	−1.35%									
8	842	0.999	−0.40%				NIR	803	0.8%	NIR	834	0.78%
8A	865	1.027	−0.84%	NR	865	−0.28%						
9	945	NA	NA									
10	1375	NA	NA	Cirrus	1373	NA						
11	1610	0.998	−0.40%	SWIR1	1610	−0.30%				SWIR	1610	−0.21%
12	2190	0.973	−0.12%	SWIR2	2200	0.28%						

4.2. RadCalNet

Figure 3 shows the obtained average ratios and spanned ±1 standard deviation (σ) range for all sensors over the three RadCalNet sites. It follows that the ratios generally increase with wavelength over all sites, but that patterns for the various sensors deviate significantly over the three sites.

Over LCFR, deviations between the ratios obtained for the various sensors are largest in the 0.6–0.8 µm range. The PROBA-V RED band exhibits a ratio of 0.87, while for the other sensors the ratios are ~0.95–1.00. It should be noted that the LCFR site is less homogeneous than the RVUS and GONA sites, with sparse vegetation cover.

Over GONA, all sensors have ratios roughly between 0.95 and 1.00 from ~0.45–0.85 µm and these gradually increase towards ~1.02, with the PROBA-V SWIR band being slightly higher (1.04). Further, it can be seen that the ratio variation is much smaller than for LCFR.

Similar to LCFR, large differences are observed over RVUS, as can be seen in Figure 3. The most significant differences to be noted are that Deimos-1 has ratios significantly lower than 1.0, while these

ratios over LCFR are within the 0.99–1.01 range. Further, the ratios for S2B are significantly larger than those for S2A throughout the entire VNIR and SWIR spectral ranges. This is in contrast with the ratios obtained over GONA and LCFR, which exhibit similar values, S2A being slightly larger than S2B, respectively.

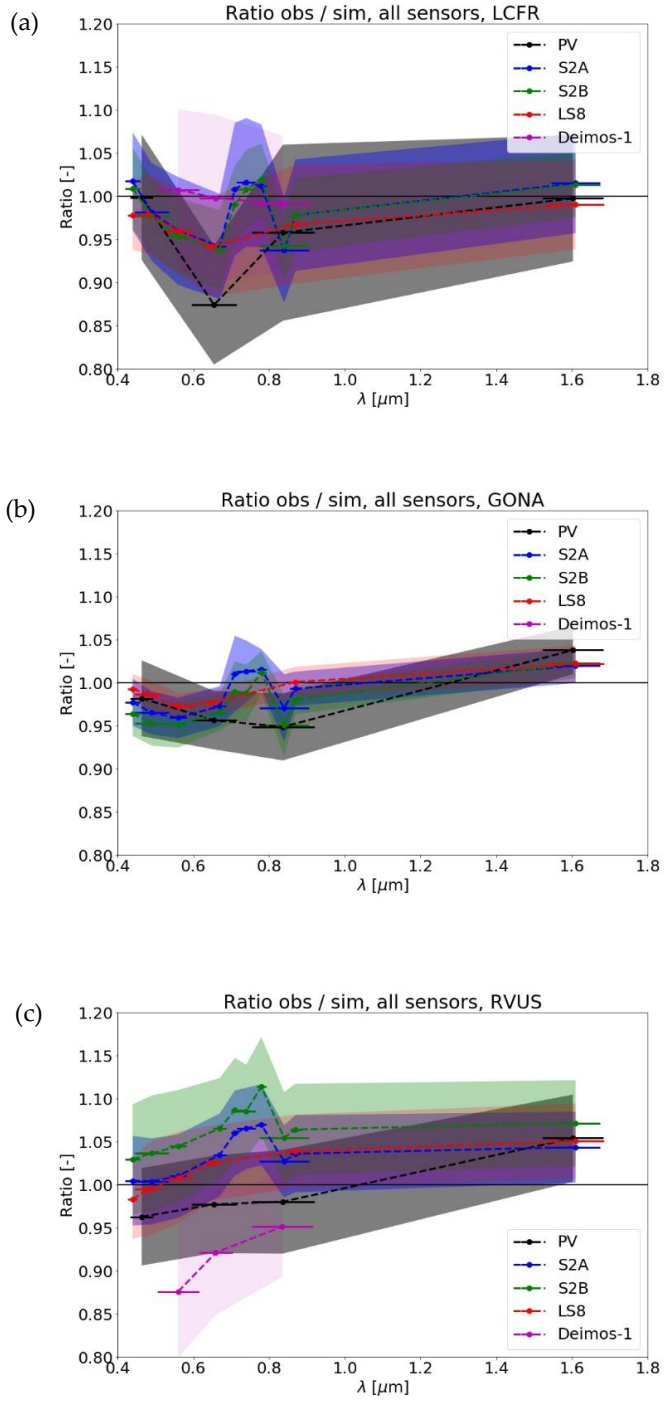

Figure 3. Ratio between the observed and RadCalNet-simulated TOA reflectances as a function of wavelength for PROBA-V (PV), Sentinel-2A (S2A), Sentinel-2B (S2B), Landsat 8 (LS8), and Deimos-1 over La Crau (LCFR) (top panel, (**a**), Gobabeb (GONA) (middle panel, (**b**), and Railroad Playa (RVUS) (bottom panel, (**c**). The shaded areas denote the ±1 standard deviation (σ) of the obtained ratios. Note that no Deimos-1 data were available for GONA.

In order to assess whether BRDF effects could play a role in the obtained results, polar plots of the viewing and illumination geometries for S2A, S2B, PROBA-V, and Deimos-1 were made for LCFR, RVUS, and GONA. These plots are shown in Figures 4–6, left columns. Note that over GONA no Deimos-1 data were available. The plots shown that only Landsat-8 observes the various sites under almost nadir viewing conditions (i.e., VZA < 1°), while for S2A and S2B the VZA is generally <10° and has a low variation, similar to LS8. Figures 5 and 6 clearly show that, over LCFR and RVUS, the viewing azimuth angle (VAA) for S2A and S2B is either ~135° or ~270°. For Deimos-1, the VAA alternates between ~80° and ~280°, while for PROBA-V, the VAA range changes more continuously between ~100° and ~280°. The GONA site is always observed by S2A and S2B under similar viewing conditions.

To further analyze the impact of the changing viewing azimuth angle, we divided the ratios of observed/RadCalNet-simulated TOA reflectances into two groups based on the observation VAA: VAA < 180° and VAA > 180°. These subsets are presented as box-whisker plots for the RED spectral range in Figures 4–6, right columns. For all investigated sensors over LCFR and RVUS, it can clearly be seen that the median and the upper and lower quartiles of the ratio distribution are generally higher for VAA < 180° than for VAA > 180°. These differences contribute considerably to the rather large variation in the RadCalNet ratios for each sensor. As a result, the variation in the ratios obtained for one sensor (the *intra-sensor* variation) is greater than between the sensors (the *inter-sensor* variation). Note that no results for Deimos-1 could be established over GONA.

To further exemplify the large *intra-sensor* variation, Figure 7 shows the TOA reflectance measured by S2A and S2B B4 (0.665 µm) over the RVUS site. The plot includes all cloud-free observations over the site, including observations without matchups with RadCalNet. Similar to Figures 4–6, a distinction is made between observations with VAA < 180° and with VAA > 180°. A clear difference in the TOA reflectance depending on the VAA can be seen once again. This difference is significantly greater than the differences observed between S2A and S2B.

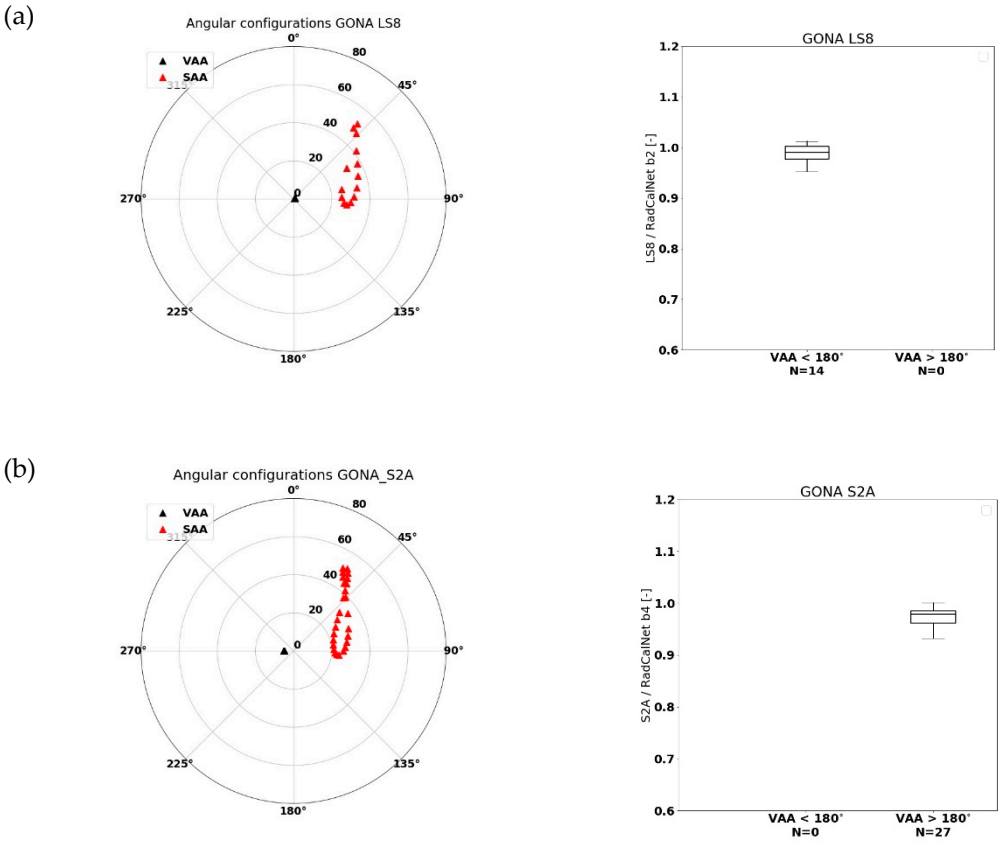

Figure 4. *Cont.*

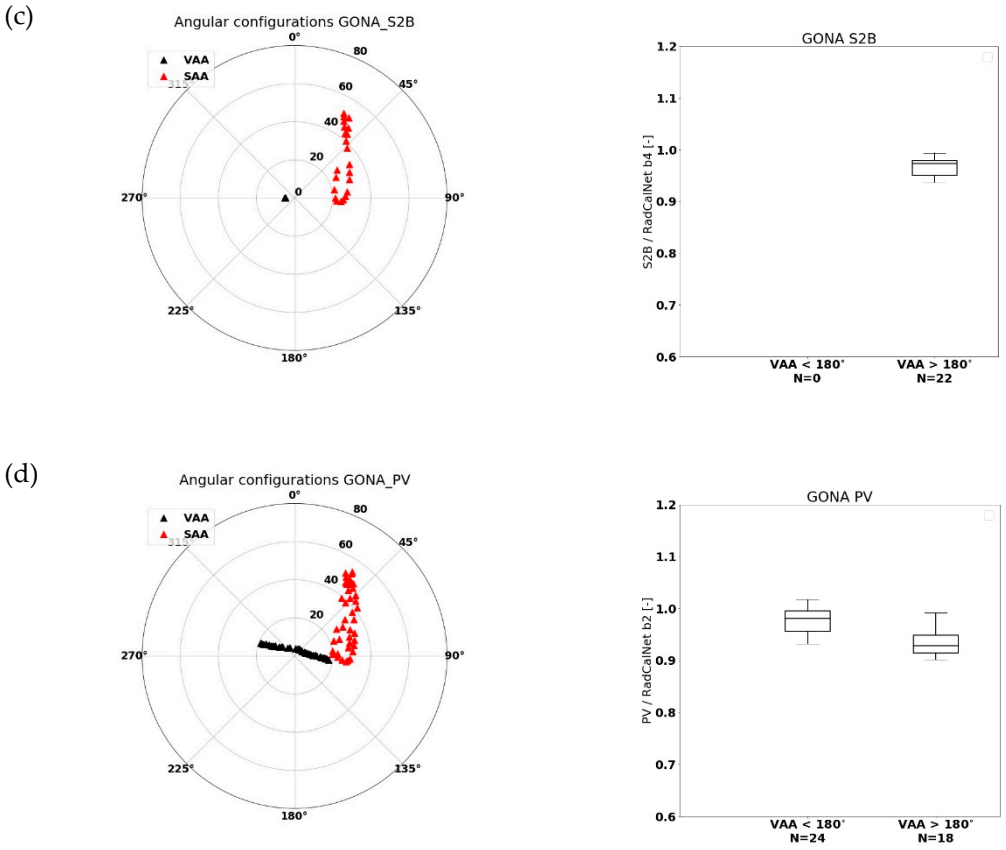

Figure 4. (left) Observation and illumination geometries for LS8 (**a**), S2A (**b**), S2B (**c**), and PROBA-V (**d**) over GONA. The viewing zenith and viewing azimuth angles (VZA and VAA) are represented by black triangles, while the solar zenith and solar azimuth angles (SZA and SAA) are denoted by red triangles. Zenith angles are plotted along the circle's radians and increase from the center going outwards. Azimuth angles start at 0° (North), increasing clockwise. (right) Box-whisker plots for the RED channel of the observed/Radcalnet-simulated TOA reflectance ratios over GONA. Results are divided into classes with VAA < 180° and VAA > 180°. The horizontal line represents the median value, whereas the lower and upper box boundaries denote the 25th and 75th percentiles, respectively. Lower and upper whiskers represent the 5th and 95th percentiles, respectively.

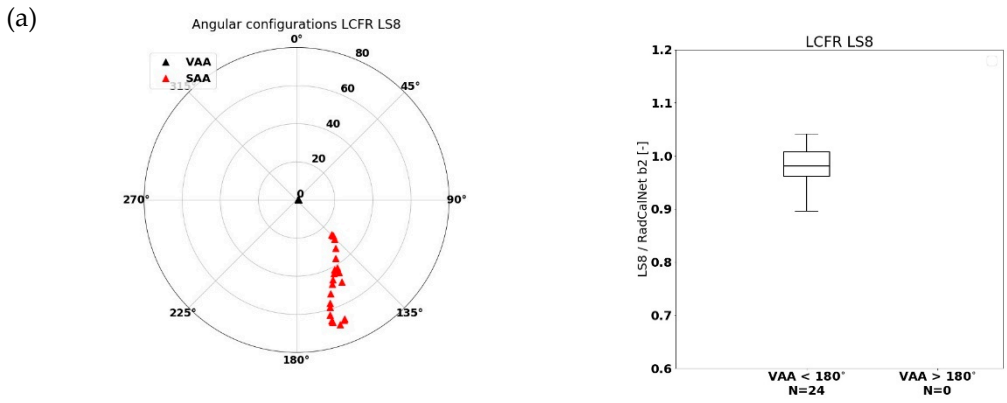

Figure 5. *Cont.*

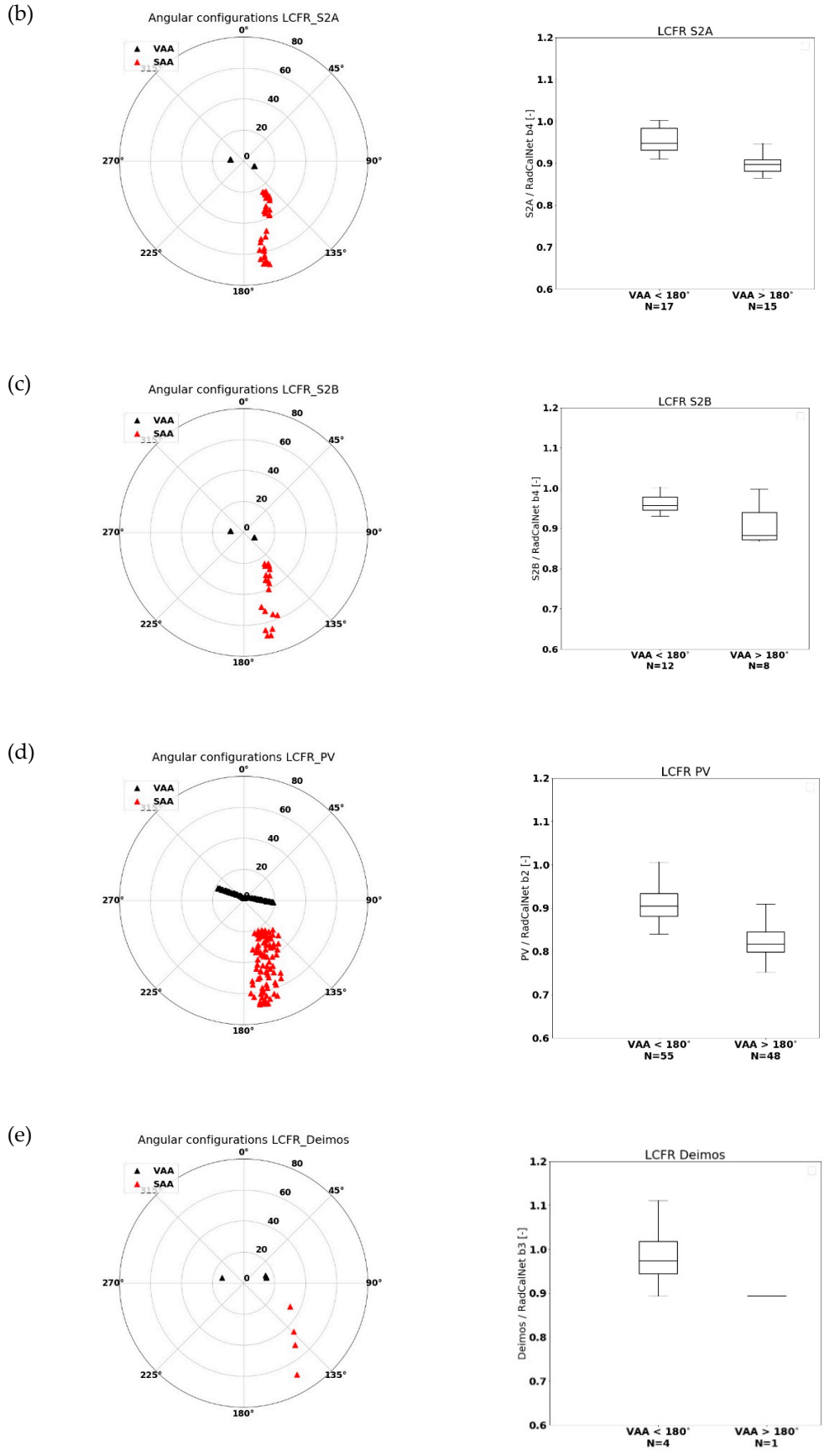

Figure 5. Similar to Figure 4, but for LCFR. Note that over this site subfigure (**e**), containing results for Deimos-1, is included.

(a)

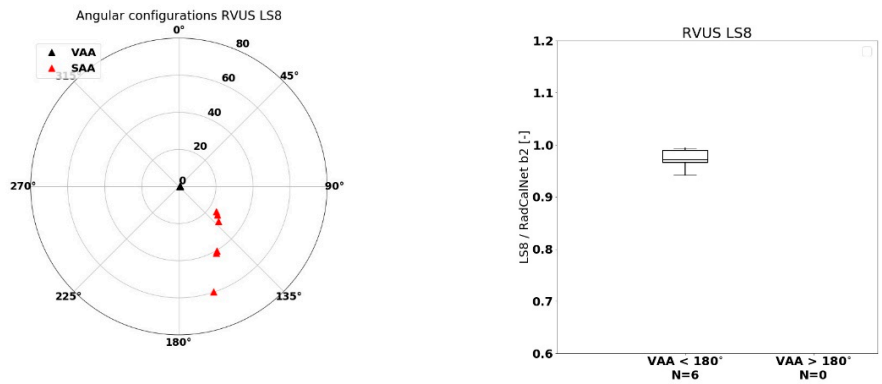

(b)

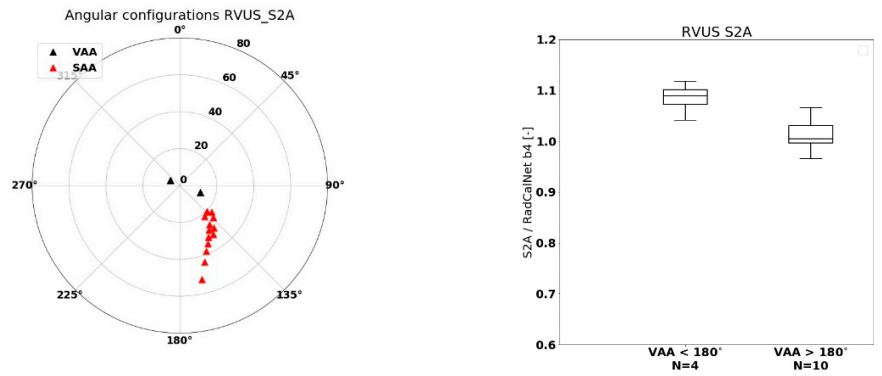

(c)

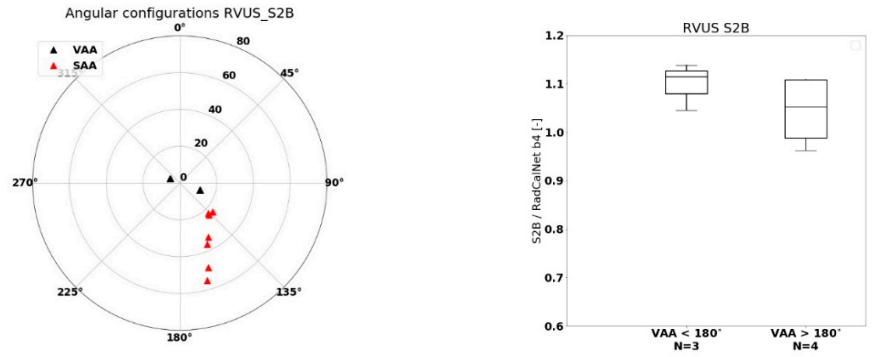

(d)

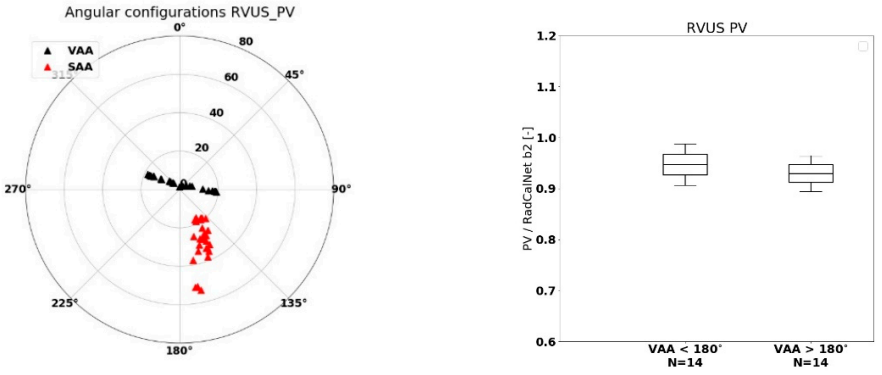

Figure 6. *Cont.*

(e)

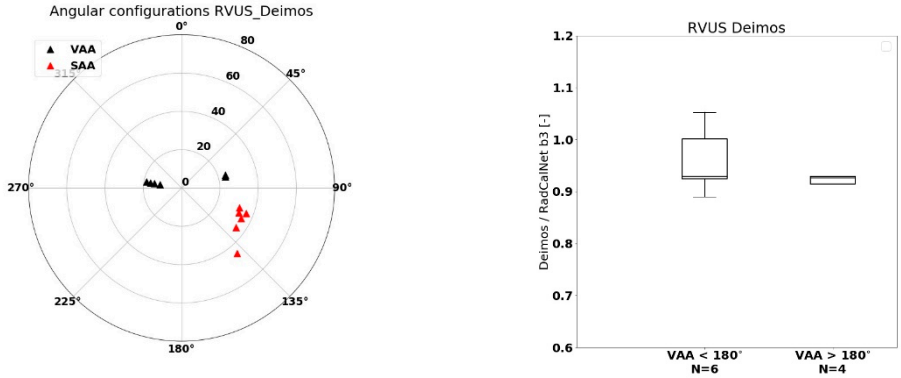

Figure 6. Similar to Figure 4, but for RVUS. Note that over this site subfigure (**e**), containing results for Deimos-1, is included.

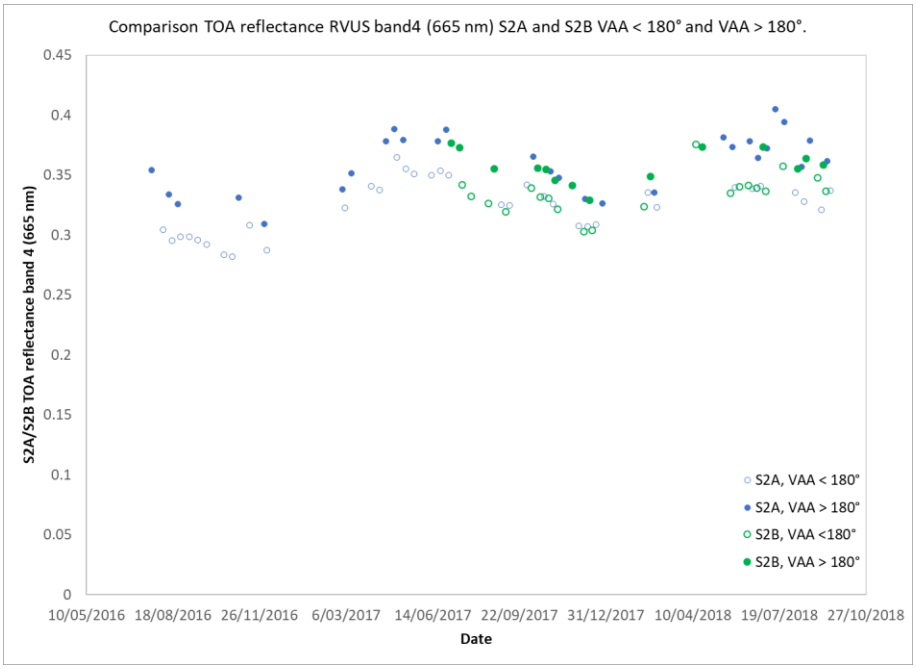

Figure 7. TOA measured B4 (0.665 µm) reflectance values of S2A (blue dots) and S2B (green dots) over the RVUS site. A distinction is made between observations with VAA < 180° (open circles) and with VAA > 180° (filled circles).

5. Discussion

The Libya-4 OSCAR method produces cross-calibration results that are more consistent and statistically robust compared to the those from the RadCalNet inter-comparison, for a number of reasons. As shown in Figures 4–7, BRDF effects strongly influence the RadCalNet results. These effects are accounted for in the OSCAR Libya-4 results through the incorporation of a BRDF model. Furthermore, no matchups with in-situ measurements are required for the OSCAR Libya-4 method. As a result, more observations were obtained in the analyses than for the individual RadCalNet sites, thereby producing results that are statistically more robust. Although overall the largest number of matchups are retrieved for the LCFR site, the results for all sensors show large error bars for this site. References [23,24] also reported on the difficulty of retrieving accurate results over the LCFR site. The large variation in the calibration results obtained over this site may be related to the site's heterogeneity, including sparse vegetation. Furthermore, due to this vegetation coverage, the convolution of the RadCalNet TOA reflectance simulations, provided at 10 nm resolution, to the

sensors' spectral bands might contain a larger uncertainty for sensors with broad spectral bands that partly cover the red edge spectral region. This might explain the deviating RadCalNet results for the PROBA-V RED band observed for the LCFR site.

The calibration results obtained over the Libya-4 site using the OSCAR methodology confirm the slight bias between S2B and S2A as observed by [23,25], with S2B having slightly lower TOA reflectance values than S2A. The strong consistency between S2 and LS8 as reported in [23,25,26], with a slightly greater difference for the LS8 CA band (Band1, 0.443 µm) is also confirmed here. To our knowledge, cross-calibration results for Deimos-1 and PROBA-V with respect to S2 and LS8 have not been published before. In [27], PROBA-V was compared against MERIS, and strong consistency (within 2.5%) was indicated.

6. Conclusions

This work focused on the assessment of radiometric differences in the TOA signal provided by PROBA-V, Sentinel-2A and Sentinel-2B, Landsat-8, and Deimos-1. The work has been performed in the frame of the BELHARMONY project, which aims to assess and to improve multi-sensor high resolution time series consistency.

Libya-4 OSCAR desert calibration results for LS8, PROBA-V, Deimos-1, S2A, and S2B agree to within ±2% for comparable spectral bands, with the exception of the Deimos-1 Green band, for which a slightly greater difference of approximately −3.5% is observed. S2A is slightly brighter than S2B for most bands. Results confirm that all sensors investigated are well calibrated and that *inter-sensor* differences are minor, at least over the bright Libya-4 site.

No consistent results could be obtained over the three RadCalNet sites for the sensors investigated. In addition to the number of matchups being rather limited to make statistically robust conclusions, BRDF effects significantly influence the observed results, as many of the satellite observations are made under non-nadir conditions. Even for slightly off-nadir VZAs of ~7°, a difference in the TOA measured reflectance values over RVUS and LCFR could be observed between Eastern and Western viewing directions. Due to these BRDF effects, the variation in the obtained ratios for one sensor (the *intra-sensor* variation) is larger than that between the sensors (the *inter-sensor* variation). In order to diminish this *intra-sensor* variation and to draw firmer conclusions, the BRDF characterizations for all RadCalNet sites must additionally be incorporated into the RadCalNet simulations and made available in the user distribution portal.

Author Contributions: S.S. designed the structure of the paper, performed the Libya-4 analyses, and supervised the RadCalNet analyses. E.W. carried out the RadCalNet analyses and co-wrote the paper.

Funding: This research was funded by the Belgian Science Policy Office (Belspo) through the Stereo program (Belharmony project) (Contract number: NR SR/00/356).

Acknowledgments: The authors thank RadCalNet and the site owners for establishing and maintaining the sites and distributing the data through the portal.

Conflicts of Interest: The authors declare no conflict of interest. The funders had no role in the design of the study; in the collection, analysis, or interpretation of data; in the drafting of the manuscript, or in the decision to publish the results.

References

1. Harmonization of Multi-Mission High Resolution Time Series: Application to BELAIR. Available online: https://belharmony.vito.be (accessed on 16 July 2019).
2. Cao, C.; Weinreb, M.; Xu, H. Predicting simultaneous nadir overpasses among polar-orbiting meteorological satellites for the intersatellite calibration of radiometers. *J. Atmos. Ocean. Technol.* **2004**, *21*, 537–542. [CrossRef]
3. Gao, H.; Gu, X.; Yu, T.; Liu, L.; Sun, Y.; Xie, Y.; Liu, Q. Validation of the calibration coefficient of the GaoFen–1 PMS sensor using the Landsat–8 OLI. *Remote Sens.* **2016**, *8*, 132. [CrossRef]

4. Czapla-Myers, J.; McCorkel, J.; Anderson, N.; Thome, K.; Biggar, S.; Helder, D.; Aaron, D.; Leigh, L.; Mishra, N. The ground-based absolute radiometric calibration of Landsat 8 OLI. *Remote Sens.* **2015**, *7*, 600–626. [CrossRef]
5. Govaerts, Y.; Sterckx, S.; Adriaensen, S. Use of simulated reflectances over bright desert target as an absolute calibration reference. *Remote Sens. Lett.* **2013**, *4*, 523–531. [CrossRef]
6. Mishra, N.; Helder, D.; Angal, A.; Choi, J.; Xiong, X. Absolute Calibration of Optical Satellite Sensors Using Libya 4 Pseudo Invariant Calibration Site. *Remote Sens.* **2014**, *6*, 1327–1346. [CrossRef]
7. Test Sites Catalog. Available online: https://calval.cr.usgs.gov/apps/test_sites_catalog (accessed on 16 July 2019).
8. Dierckx, W.; Sterckx, S.; Benhadj, I.; Livens, S.; Duhoux, G.; Van Achteren, T.; Francois, M.; Mellab, K.; Saint, G. PROBA-V mission for global vegetation monitoring: Standard products and image quality. *Int. J. Remote Sens.* **2014**, *35*, 2589–2614. [CrossRef]
9. Sterckx, S.; Benhadj, I.; Duhoux, G.; Livens, S.; Dierckx, W.; Goor, E.; Adriaensen, S.; Heyns, W.; Van Hoof, K.; Strackx, G.; et al. The PROBA-V mission: Image processing and calibration. *Int. J. Remote Sens.* **2014**, *35*, 2565–2588. [CrossRef]
10. Toté, C.; Swinnen, E.; Sterckx, S.; Adriaensen, S.; Benhadj, I.; Iordache, M.; Bertels, L.; Kirches, G.; Stelzer, K.; Dierckx, W.; et al. Evaluation of PROBA-V Collection 1: Refined Radiometry, Geometry, and Cloud Screening. *Remote Sens.* **2018**, *10*, 1375. [CrossRef]
11. Lozano, F.J.; Romo, A.; Moclan, C.; Gil, J.; Pirondini, F. The DEIMOS-1 mission: Absolute and relative calibration activities and radiometric optimization. In Proceedings of the 2012 IEEE International Geoscience and Remote Sensing Symposium, Munich, Germany, 22–27 July 2012; pp. 4754–4757. [CrossRef]
12. Markham, B.; Barsi, J.; Kvaran, G.; Ong, L.; Kaita, E.; Biggar, S.; Czapla-Myers, J.; Mishra, N.; Helder, D. Landsat-8 Operational Land Imager Radiometric Calibration and Stability. *Remote Sens.* **2014**, *6*, 12275–12308. [CrossRef]
13. Rahman, H.; Pinty, B.; Verstraete, M.M. Coupled Surface-Atmosphere Reflectance (CSAR) model 2. Semiempirical surface model usable with NOAA advanced very high resolution radiometer data. *J. Geophys. Res.* **1993**, *98*, 20791–20801. [CrossRef]
14. Govaerts, Y.M.; Clerici, M. Evaluation of radiative transfer simulations over bright desert calibration sites. *IEEE Trans. Geosci. Remote* **2004**, *42*, 176–187. [CrossRef]
15. Holben, B.N.; Eck, T.F.; Slutsker, I.; Tanre, D.; Buis, J.P.; Setzer, A.; Vermote, E.; Reagan, J.A.; Kaufman, Y.J.; Nakajima, T.; et al. AERONET—A federated instrument network and data archive for aerosol characterization. *Remote Sens. Environ.* **1998**, *66*, 1–16. [CrossRef]
16. Govaerts, Y.M. Sand Dune Ridge Alignment Effects on Surface BRF over the Libya-4 CEOS Calibration Site. *Sensors* **2015**, *15*, 3453–3470. [CrossRef]
17. Bacour, C.; Briottet, X.; Bréon, F.-M.; Viallefont-Robinet, F.; Bouvet, M. Revisiting Pseudo Invariant Calibration Sites (PICS) Over Sand Deserts for Vicarious Calibration of Optical Imagers at 20 km and 100 km Scales. *Remote Sens.* **2019**, *11*, 1166. [CrossRef]
18. Bialek, A.; Greenwell, C.; Lamare, M.; Meygret, A.; Marcq, S.; Lachérade, S.; Woolliams, E.; Berthelot, B.; Bouvet, M.; King, M.; et al. New radiometric calibration site located at Gobabeb, Namib desert. In Proceedings of the 2016 IEEE International Geoscience and Remote Sensing Symposium (IGARSS), Beijing, China, 10–15 July 2016; pp. 6094–6097. [CrossRef]
19. Czapla-Myers, J.; McCorkel, J.; Anderson, N.; Biggar, S. Earth-observing satellite intercomparison using the Radiometric Calibration Test Site at Railroad Valley. *J. Appl. Remote. Sens.* **2017**, *12*. [CrossRef]
20. RadCalNet Radiometric Calibration Network Portal. Available online: https://www.radcalnet.org/#!/ (accessed on 16 July 2019).
21. Marcq, S.; Meygret, A.; Bouvet, M.; Fox, N.; Greenwell, C.; Scott, B.; Berthelot, B.; Besson, B.; Guilleminot, N.; Damiri, B. New RadCalNet site at Gobabeb Namibia: Installation of the instrumentation and first satellite calibration results. In Proceedings of the IGARSS 2018—2018 IEEE International Geoscience and Remote Sensing Symposium, Valencia, Spain, 22–27 July 2018; pp. 6444–6447.
22. Czapla-Myers, J.; Ong, L.; Thome, K.; McCorkel, J. Validation of EO-1 Hyperion and Advanced Land Imager Using the Radiometric Calibration Test Site at Railroad Valley, Nevada. *IEEE J. Sel. Top. Appl.* **2016**, *9*, 816–826. [CrossRef]

23. Revel, C.; Lonjou, V.; Marcq, S.; Desjardins, C.; Fougnie, B.; Coppolani-Delle, C.; Guilleminot, N.; Lacamp, A.; Lourme, E.; Miquel, C.; et al. Sentinel-2A and 2B absolute calibration monitoring. *Eur. J. Remote Sens.* **2019**, *52*, 122–137. [CrossRef]
24. Jing, X.; Leigh, L.; Teixeira Pinto, C.; Helder, D. Evaluation of RadCalNet Output Data Using Landsat 7, Landsat 8, Sentinel 2A, and Sentinel 2B Sensors. *Remote Sens.* **2019**, *11*, 541. [CrossRef]
25. Helder, D.; Markham, B.; Morfitt, R.; Storey, J.; Barsi, J.; Gascon, F.; Clerc, S.; LaFrance, B.; Masek, J.; Roy, D.P.; et al. Observations and Recommendations for the Calibration of Landsat 8 OLI and Sentinel 2 MSI for Improved Data Interoperability. *Remote Sens.* **2018**, *10*, 1340. [CrossRef]
26. Barsi, J.; Alhammoud, B.; Czapla-Myers, J.; Gascon, F.; Haque, M.H.; Maewmanee, M.; Leigh, L.; Markham, B. Sentinel-2A MSI and Landsat-8 OLI Radiometric Cross Comparison. *Eur. J. Remote Sens.* **2018**, *51*, 822–837. [CrossRef]
27. Sterckx, S.; Adriaensen, S.; Dierckx, W.; Bouvet, M. In-Orbit Radiometric Calibration and Stability Monitoring of the PROBA-V Instrument. *Remote Sens.* **2016**, *8*, 546. [CrossRef]